Assessing nanoparticle colloidal stability with single-particle inductively coupled plasma mass spectrometry (SP-ICP-MS)

Nathan D. Donahue[1] · Emmy R. Francek[1] · Emi Kiyotake[1] · Emily E. Thomas[1] · Wen Yang[1] · Lin Wang[1] · Michael S. Detamore[1,2] · Stefan Wilhelm[1,2,3]

Abstract

Biological interactions, toxicity, and environmental fate of engineered nanoparticles are affected by colloidal stability and aggregation. To assess nanoparticle aggregation, analytical methods are needed that allow quantification of individual nanoparticle aggregates. However, most techniques used for nanoparticle aggregation analysis are limited to ensemble measurements or require harsh sample preparation that may introduce artifacts. An ideal method would analyze aggregate size in situ with single-nanoparticle resolution. Here, we established and validated single-particle inductively coupled plasma mass spectrometry (SP-ICP-MS) as an unbiased high-throughput analytical technique to quantify nanoparticle size distributions and aggregation in situ. We induced nanoparticle aggregation by exposure to physiologically relevant saline conditions and applied SP-ICP-MS to quantify aggregate size and aggregation kinetics at the individual aggregate level. In situ SP-ICP-MS analysis revealed rational surface engineering principles for the preparation of colloidally stable nanoparticles. Our quantitative SP-ICP-MS technique is a platform technology to evaluate aggregation characteristics of various types of surface-engineered nanoparticles under physiologically relevant conditions. Potential widespread applications of this method may include the study of nanoparticle aggregation in environmental samples and the preparation of colloidally stable nanoparticle formulations for bioanalytical assays and nanomedicine.

Keywords Nanoparticle · Single-particle ICP-MS · Elemental analysis · Aggregation · Colloidal stability · Surface chemistry

Introduction

In contrast to their corresponding bulk materials, nanoparticles exhibit unique size-dependent optical, electric, magnetic, and biological properties that are exploited in various applications, including catalysis, display technology, energy generation and storage, and medicine [1–3]. Therefore, the effective application of nanoparticles requires precise and accurate quantification of nanoparticle size, size distributions, colloidal stability, and aggregation. Aggregation is a common nanoparticle transformation that changes nanoparticle size and surface chemistry leading to alterations in cellular uptake, biodistribution, pharmacokinetics, toxicity, and overall fate [4–7]. Conventional analytical methods for measuring nanoparticle size and aggregation are often performed in batch mode and only provide population-averaged results.

For a given nanoparticle sample, such averaged results can mask population heterogeneities (e.g., aggregation) that ultimately may affect the performance of nanoparticles in their respective applications. Examples of such batch analytical methods for nanoparticle size characterization include spectroscopy techniques, light scattering, differential centrifugal sedimentation, field flow fractionation, atomic force microscopy, and size exclusion chromatography [8–10]. While batch analytical methods are well-established and widespread, they are unable to measure individual nanoparticle and aggregate

✉ Stefan Wilhelm
stefan.wilhelm@ou.edu

1 Stephenson School of Biomedical Engineering, University of Oklahoma, Norman, OK 73019, USA

2 Institute for Biomedical Engineering, Science, and Technology (IBEST), Norman, OK 73019, USA

3 Stephenson Cancer Center, Oklahoma City, OK 73104, USA

sizes. This limitation results in an inability to accurately assess the true size heterogeneity for a given nanoparticle population. An ideal analytical method should rapidly and precisely provide size information at the individual particle level. Several single-particle resolution techniques are available and include electron microscopy methods, nanoparticle tracking analysis, and single-particle spectroscopy [11–13]. However, in electron microscopy, colloidal nanoparticle samples are typically analyzed after drying on support grids and require complex image analysis algorithms to pinpoint clusters of nanoparticles over multiple fields of view [14]. Meanwhile, light scattering techniques, such as nanoparticle tracking analysis, could potentially overestimate aggregate size by reporting hydrodynamic diameters and be skewed by changes in a dispersion's viscosity, refractive index, and/or temperature [15].

One salient example of single-particle analytical techniques that is able to detect and quantify individual nanoparticles via elemental analysis is single-particle inductively coupled plasma mass spectrometry (SP-ICP-MS) [16, 17]. In a SP-ICP-MS experiment, one nanoparticle at a time is introduced into the ICP-MS instrument via a microfluidic system with controlled flow rate. Each individual nanoparticle is then atomized and ionized by an argon plasma, and the resulting ion plume is analyzed by a quadrupole-based mass analyzer to quantify the corresponding nanoparticle mass. This SP-ICP-MS technique has been applied to quantify a variety of nanoparticle types and is being applied to quantify element concentrations inside intact individual cells [17–19].

Our motivation for studying nanoparticle aggregation via SP-ICP-MS is driven by the importance of evaluating nanoparticle colloidal stability and how this stability can be affected by nanoparticle surface engineering strategies [20–23]. Understanding nanoparticle stability with single-particle resolution is critical for determining the environmental and biological impact of nanoparticles [24–26]. Aggregation and colloidal stability are therefore important parameters affecting nanoparticle physicochemical properties that need to be characterized when studying interactions between nanoparticles and ecological and biological systems, including cells, tissues, and organs [27–29].

In the current study, we analyzed the size distributions of various in-house synthesized gold nanoparticles with conventional batch and single-particle resolution techniques. We demonstrated and validated SP-ICP-MS to precisely quantify engineered nanoparticles consisting of multiple sizes and shapes. Additionally, we applied SP-ICP-MS to quantify engineered nanoparticle aggregation characteristics with single-particle resolution in situ. These nanoparticle aggregates are clusters of multiple individual nanoparticles and detected by the ICP-MS as a single event exhibiting a mass that corresponds to a single-nanoparticle mass multiplied by the number of nanoparticles per aggregate [30]. This approach requires nanoparticles with narrow size distribution, and

hence narrow mass distribution, which is typically the case for engineered nanoparticles.

Our single-particle analytical approach provides a quantitative tool for probing nanoparticle surface chemistries and corresponding colloidal stability in situ under physiologically relevant conditions. This reported SP-ICP-MS procedure could be widely applied to study nanoparticle environmental fate and to probe and establish surface engineering approaches leading to nanoparticle formulations with controlled colloidal stability to use in bioanalytical assays and nanomedicine.

Experimental section

Gold nanoparticle synthesis

For all synthesis steps, glass Erlenmeyer flasks were cleaned before synthesis with Aqua Regia, i.e., 3:1 (v/v) mixture of hydrochloric acid (Sigma-Aldrich, ACS reagent, 37%, St. Louis, MO) and nitric acid (Sigma-Aldrich, ACS reagent, 70%) to remove potential contaminants. Gold nanoparticles (AuNPs) with a nominal size of 16 nm were synthesized according to a previously published protocol [20]. To synthesize 30- and 55-nm quasi-spherical AuNPs, a seed-mediated synthesis protocol developed by Perrault and Chan was adopted using 16-nm AuNPs as seed nanoparticles [31]. Gold nanorods were synthesized according to previously published reports [32, 33]. Detailed procedures are provided in the Electronic Supplementary Material (ESM).

Nanoparticle characterization

The ZetaSizer Nano ZS (Malvern, UK) was used to measure the z-average hydrodynamic diameter of nanoparticles based on dynamic light scattering (DLS) and zeta potential based on electrophoretic mobility. Transmission electron micrographs (TEM) were taken by a 200-kV field emission JEOL2010F microscope (JEOL, USA) equipped with a Direct Electron DE-12 camera (Direct Electron, USA). ImageJ (NIH) software was used to determine the diameters of AuNPs in the TEM images. An Agilent Cary 5000 UV-Vis-NIR spectrophotometer (Agilent, USA) was used to measure the visible spectrum of AuNPs from 400 to 700 nm in 1.5-mL PMMA cuvettes.

Nanoparticle PEGylation

Surface modifications of AuNPs were performed using HS(PEG)5kDa-methoxy (Laysan Bio, USA) and using a previously reported procedure [20]. Detailed procedures are provided in the ESM. The successful conjugation of different PEG densities on the AuNPs was confirmed by DLS, zeta potential, and gel electrophoresis.

SP-ICP-MS instrument setup

All SP-ICP-MS measurements were performed using the NexION 2000 B ICP-MS (PerkinElmer, USA) fitted with a commercially available high-efficiency sample introduction system pictured in ESM Fig. S1. The ICP-MS instrument was operated using the conditions summarized in ESM Table S2. The SP-ICP-MS particle transport efficiency was determined using commercially available polystyrene microparticles (~3 μm in diameter) doped with Lu175 (Fluidigm, USA). A transport efficiency of $58.5 \pm 3.9\%$ was determined. With the same instrument setup, Merrifield et al. demonstrated that transport efficiencies of polystyrene microparticles and standard AuNPs do not statistically differ [34]. Typical transport efficiencies for single-particle/cell ICP-MS systems can range between 9 and 70% [35–37]. Our system's transport efficiency is on the higher end of the range reported in the literature due to the high-efficiency nebulizer and spray chamber which minimize sample loss and ensure robust sample introduction to the ICP-MS. With high transport efficiency, micro-scale dwell time, no settling time, and low nebulizer gas flow, the instrument was optimized to quantify transient ion signals from nanoparticles. Next, the mass detector was set to only analyze Au197 signal and the ICP-MS was calibrated with dissolved gold ion standards made from a stock solution consisting of 1000 μg/mL (Au) ICP single-component standard in 2% HCl (high purity standards 100021-2-100, USA) via serial dilution. With our dissolved Au calibration curve, the measured pulse intensity from an ion plume was then used to back-calculate nanoparticle mass as described by Pace et al. [38].

Nanoparticle sample preparation for SP-ICP-MS

To accurately analyze nanoparticle mass distributions with SP-ICP-MS, nanoparticle solutions were diluted to 1.66×10^{-16} M in nanopure water 18.2 MΩ cm from the initial concentration determined by UV-Vis. This concentration of 1.66×10^{-16} M was chosen as this is approximately 1×10^{5} particles mL^{-1}, which can virtually eliminate the probability of overlapping events from multiple nanoparticles during a single dwell time of 50 μs based on the Poisson distribution outlined by Pace et al. [39].

For making a 1:1 mixture of nanoparticles, 50 μL of 1.66×10^{-15} M of each nanoparticle size was added to 900 μL of nanopure water 18.2 MΩ cm and analyzed immediately on SP-ICP-MS. For gold nanorod analysis, 2 μL of the solution containing citrate-coated nanorods was diluted into 10 mL of nanopure water 18.2 MΩ cm. This diluted mixture of nanorods was diluted again by taking 1 μL and adding that to 999 μL of nanopure water and immediately analyzed on SP-ICP-MS. For measuring T_0 of aggregation on SP-ICP-MS, the concentrated nanoparticle and salt mixture were diluted to 1.66×10^{-16} M and analyzed immediately after salt addition. For the later time point, the concentrated nanoparticles remained in salt and after 1 h had elapsed, the mixture was diluted to 1.66×10^{-16} M and analyzed immediately. For all nanoparticle samples, the mass detector was set to analyze Au197 signal.

SP-ICP-MS data acquisition and analysis

All nanoparticle events were collected within 60 s. Syngistix software (PerkinElmer, USA) was used in SP-ICP-MS mode to acquire single-particle elemental analysis data. Statistical analyses were performed with GraphPad Prism (GraphPad, USA).

Results and discussion

Nanoparticle synthesis and characterization

We synthesized three different batches of quasi-spherical citrate-coated colloidal AuNPs in house with nominal diameters of (i) 16 nm, (ii) 30 nm, and (iii) 55 nm, and characterized these AuNPs with three commonly used analytical techniques: (i) dynamic light scattering (DLS); (ii) UV-Vis spectrophotometry (UV-Vis); and (iii) transmission electron microscopy (TEM). Two of these methods, i.e., DLS and UV-Vis, are batch methods that analyze AuNP physicochemical and photophysical properties for an entire ensemble of nanoparticles, while TEM allows AuNP characterization at the single-nanoparticle level.

The nanoparticle hydrodynamic diameters obtained by DLS measurements are summarized in Fig. 1a. It is worth noting that hydrodynamic diameters take into account nanoparticle surface–bound ions and molecules as well as the layer of hydration around a nanoparticle surface. Hence, the synthesized 16-nm, 30-nm, and 55-nm citrate-coated AuNPs exhibited average hydrodynamic diameters of 18.0 ± 1.0 nm, 37.6 ± 2.6 nm, and 54.4 ± 3.8 nm, respectively. Our DLS results demonstrate that the nanoparticle size distributions are narrow (< 10% size deviation) with polydispersity indices (PDI) below 0.1 indicating colloidal stability without detectable nanoparticle aggregation.

Next, we used UV-Vis spectrophotometry to measure the nanoparticle size–dependent light absorption spectra of our in-house synthesized colloidal AuNPs. Observed spectra are a result of AuNP light absorption due to the surface plasmon resonance (SPR) effect and light scattering due to the particle nature of the AuNPs [40]. Since nanoparticles with diameters below 100 nm were used, light absorption rather than light scattering is the dominant factor accounting for the light extinction spectra seen in Fig. 1b [41]. Compared with smaller AuNPs, larger sized AuNPs exhibited a red-shifted light
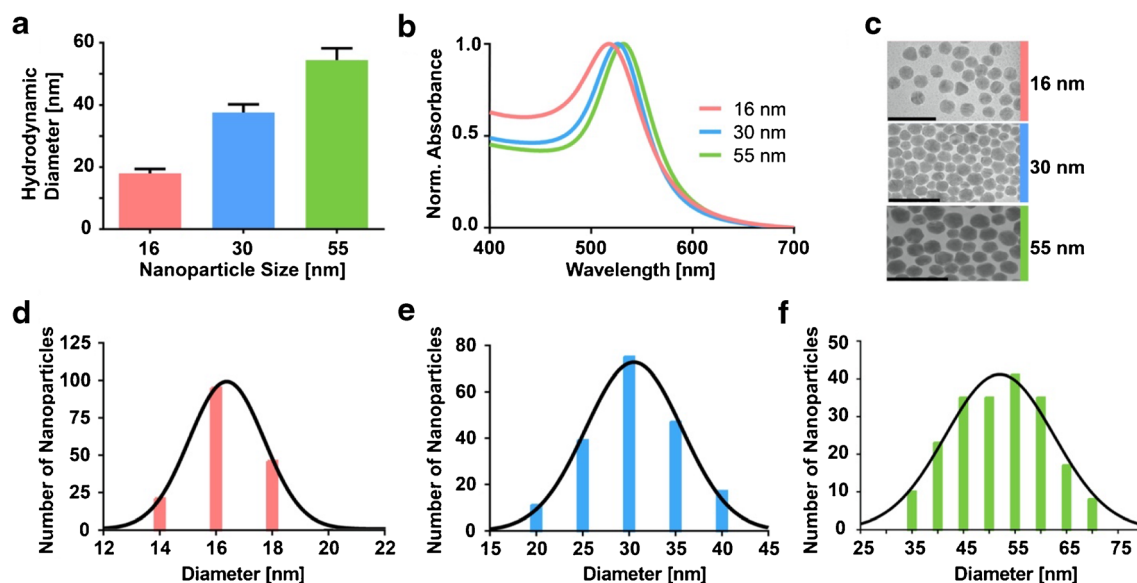
Fig. 1 Nanoparticle characterization of three different batches of citrate-coated AuNPs. **a** Hydrodynamic diameters as obtained by DLS. Bars represent mean values and standard deviation ($n = 3$). **b** UV-Vis spectrophotometry spectra. **c** Transmission electron micrographs. Scale bars indicate 50 nm, 100 nm, and 200 nm, respectively (top to bottom). **d–f** Nanoparticle size distribution histograms based on TEM image analysis using ImageJ. The AuNP distributions (black lines) were fitted using a Gaussian distribution in GraphPad Prism

absorption peak with λ_{max} 518 nm for 16-nm AuNPs, λ_{max} 526 nm for 30-nm AuNPs, and λ_{max} 532 nm for 55-nm AuNPs (Fig. 1b). This observation can be explained by nanoparticle size–dependent changes in SPR frequencies [42]. The obtained UV-Vis spectra corroborated our DLS experiments to further confirm the colloidal stability and narrow size distribution of our synthesized AuNPs. Despite the limitations associated with ensemble light-based techniques, DLS and UV-Vis provide rapid quantitative and qualitative information on nanoparticle size and colloidal stability.

Since DLS and UV-Vis spectrophotometry methods do not provide single-particle resolution, we used TEM to measure individual nanoparticles (Fig. 1c). Quantitative image analysis of TEM micrographs revealed average sizes of AuNPs of 16.3 ± 1.2 nm (16-nm sample), 30.6 ± 5.4 nm (30-nm sample), and 52.2 ± 9.1 nm (55-nm sample). The corresponding size distribution histograms are shown in Fig. 1 d–f. The TEM characterization studies confirmed our results obtained by DLS and UV-Vis methods and demonstrated that our in-house synthesized AuNPs were monodisperse without detectable nanoparticle aggregation. Although TEM provides direct images of AuNPs, it requires harsh conditions (i.e., sample drying on TEM grids, high vacuum conditions) and post-image analysis, which prevent high-throughput in situ characterization.

SP-ICP-MS of quasi-spherical nanoparticles

Next, we performed SP-ICP-MS on all three citrate-coated AuNP colloidal samples using a PerkinElmer NexION 2000 ICP-MS. The SP-ICP-MS method is an elemental analysis technique that allows mass quantification of individual nanoparticles, one nanoparticle at a time. To prepare the AuNP samples for SP-ICP-MS analysis, we quantified the corresponding nanoparticle molar concentrations of AuNP stock dispersions by UV-Vis spectrophotometry using the nanoparticle size–dependent molar decadic extinction coefficients listed in Table S1. We then diluted the AuNPs to a nanoparticle concentration of 1.66×10^{-16} M (1.0×10^5 AuNPs mL^{-1}) in nanopure water. To analyze individual AuNPs, the ICP-MS was set up and calibrated according to the parameters listed in Fig. S1 and Table S2 (see ESM).

Individual AuNPs were introduced into the ICP-MS by a commercially available microfluidics autosampler connected to a high-efficiency nebulizer and spray chamber for efficient aerosol generation of the aqueous nanoparticle dispersions (ESM Fig. S1). Individual AuNPs then pass through the argon plasma and become atomized and ionized, resulting in a transient gold ion plume that is analyzed by a quadrupole mass analyzer and detected with microsecond dwell times, which enables precise quantification of nanoparticle size [43]. The intensities of the detected gold ion plumes correspond to individual AuNP masses that were then displayed as mass histograms (Fig. 2a–c).

Based on our TEM imaging results (Fig. 1c), we approximated the shape of our in-house synthesized AuNPs to be spherical. This approximation allowed us to estimate the diameter of an individual AuNP by converting the reported SP-ICP-MS AuNP mass according to Eq. 1:

$$d \ [\text{nm}] = \sqrt[3]{\frac{6 \cdot \text{MassNP}}{\pi \cdot \rho}} \qquad (1)$$
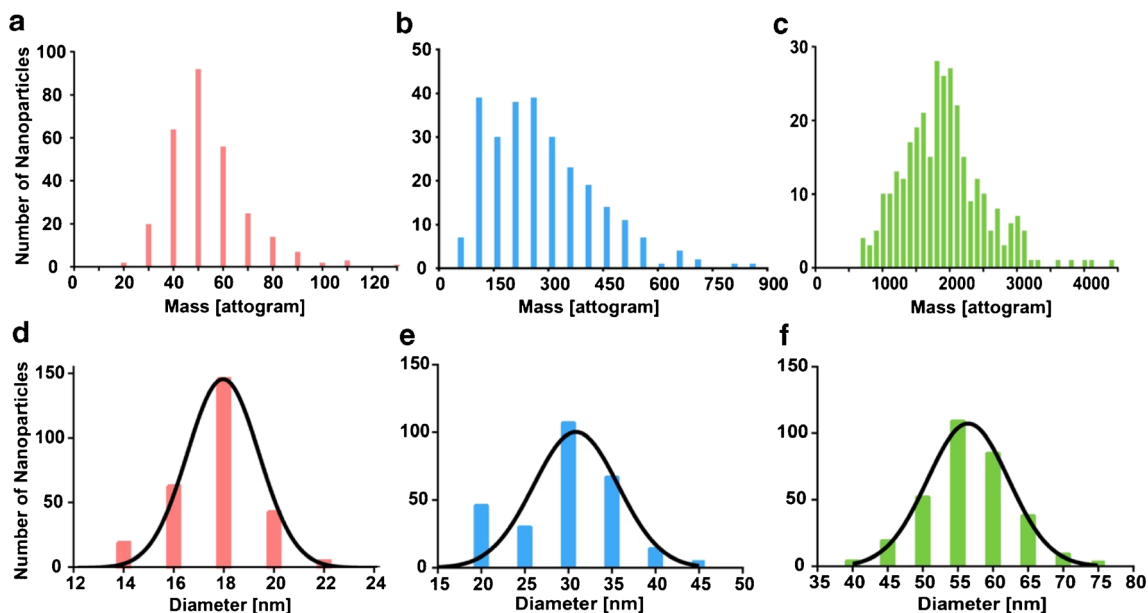
Fig. 2 Nanoparticle size characterization based on SP-ICP-MS. Panels **a**–**c** show SP-ICP-MS mass histograms for 16-nm AuNPs (**a**), 30-nm AuNPs (**b**), and 55-nm AuNPs (**c**). In panels **d**–**f**, the masses of **a**–**c** histograms are converted into corresponding nanoparticle diameters. The AuNP distributions (black lines) were fitted using a Gaussian distribution in GraphPad Prism

with MassNP as the reported SP-ICP-MS mass in [g] unit of a single individual AuNP, and ρ is the density of gold (19.3 g/cm³). The obtained SP-ICP-MS-based AuNP size distribution histograms are shown in Fig. 2 d–f.

The SP-ICP-MS method accurately determined the size distributions of the three different colloidal AuNP batches that we synthesized in house at a rate of ≥ 200 particles/min. Interestingly, with the SP-ICP-MS technique, we were able to quantify AuNPs with masses as small as 20 ag (corresponding to spherical nanoparticles with ~ 13 nm in diameter) which closely resembles the limits of detection mentioned in other SP-ICP-MS reports [44]. When compared with conventional nanoparticle characterization techniques, such as DLS, UV-Vis, and TEM (Fig. 2), SP-ICP-MS yielded overall comparable results. Table 1 provides a succinct head-to-head comparison of the results obtained from DLS, TEM, and SP-ICP-MS. All three methods provide similar nanoparticle mean diameters and standard deviations of analyzed AuNPs batches (Table 1). These results validated SP-ICP-MS as a high-throughput, accurate, in situ quantitative analytical method to determine the size distribution of individual AuNPs.

SP-ICP-MS of nanoparticle mixtures

After successfully determining the mass and size distributions of AuNPs with different sizes, we used SP-ICP-MS to differentiate between nanoparticles of different sizes in mixtures. We prepared a 1:1 mixture of in-house synthesized spherical citrate-coated 30-nm and 55-nm AuNPs. We analyzed this 1:1 nanoparticle mixture with SP-ICP-MS and observed two clearly separated nanoparticle populations in the SP-ICP-MS mass distribution histogram as well as the corresponding calculated size distribution histogram (Fig. 3). From the SP-ICP-MS analysis results of the 1:1 AuNP mixture, the 30-nm and 55-nm AuNP mean diameters were calculated to be 30.8 nm and 57.9 nm, respectively. In addition, SP-ICP-MS also accurately determined that the AuNP mixture was indeed made from a 1:1 mixture of 30-nm and 55-nm AuNPs with 268 particles determined as 30-nm AuNPs and 234 particles determined as 55-nm AuNPs. This result indicated AuNP recovery of ~ 90% from the original 1:1 mixture. We also confirmed that the mean diameters and standard deviations of the AuNPs

Table 1 Comparison of nanoparticle measurements

Sample	Hydrodynamic diameter (nm)	Nanoparticle core diameter (nm)	Mean nanoparticle mass (ag)	Calculated nanoparticle diameter (nm)
16-nm AuNPs	18.0 ± 1.0	16.3 ± 1.2	53.2 ± 16.0	17.2 ± 1.7
30-nm AuNPs	37.6 ± 2.6	30.6 ± 5.4	290.7 ± 164.4	29.7 ± 5.5
55-nm AuNPs	54.4 ± 3.8	52.2 ± 9.1	1952.1 ± 643.6	57.1 ± 6.1

Diameters and masses are provided as mean values ± standard deviation
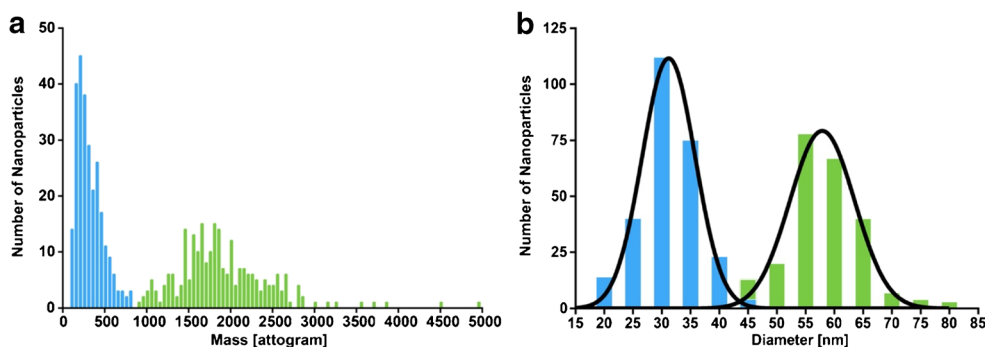
Fig. 3 SP-ICP-MS analysis of 1:1 mixture of AuNPs. **a** Mass histogram of 1:1 mixtures of 30-nm (blue population) and 55-nm (green population) AuNPs obtained by SP-ICP-MS. **b** Mass histogram from panel **a** is converted into diameter histogram. The total number of AuNPs analyzed was 502, with 268 particles determined as 30-nm AuNPs

(blue) and 234 particles determined as 55-nm (green) AuNPs by SP-ICP-MS. The AuNP distributions (black lines) were fitted using a Gaussian distribution in GraphPad Prism. The AuNP distributions were statistically significantly different based on an unpaired T test ($t = 52.28$, df = 500, $p < 0.0001$)

measured in the mixture were not different from the AuNP measurement results reported in Table 1 for pure, unmixed AuNP samples. As shown in ESM Fig. S2, the nanoparticle diameters calculated from the SP-ICP-MS analysis of the 1:1 AuNP mixture were not statistically significantly different ($p < 0.01$) compared with the pure, unmixed AuNPs. Our results confirmed that SP-ICP-MS can simultaneously and precisely measure AuNP mass distributions of multiple nanoparticle subpopulations for a given nanoparticle mixture and points to the possibility of analyzing complex nanoparticle mixtures with single-particle resolution.

SP-ICP-MS of nanorods

Next, we wondered whether SP-ICP-MS could be used for the quantitative analysis of non-spherical nanoparticles that exhibit an aspect ratio. As a model nanoparticle system, we synthesized citrate-capped gold nanorods in house. We analyzed the size distribution of the synthesized gold nanorods with TEM and quantified length and width of individual gold nanorods from corresponding micrographs with ImageJ. The average lengths and widths of the gold nanorods were 63.5 nm and 9.0 nm, respectively (ESM Fig. S3). Based on the TEM micrographs, we assumed a cylindrical geometry of the gold nanorods and estimated the average nanoparticle mass to be ~ 313 ag using Equations S1 and S2 (see ESM). We then used SP-ICP-MS to characterize individual gold nanorods from diluted aqueous dispersions. Our SP-ICP-MS analysis revealed an average nanoparticle mass of ~ 319 ag (ESM Fig. S3), which is in close agreement with the estimated mass after TEM analysis (ESM Fig. S3). Our results corroborate previous reports that SP-ICP-MS is not limited to nanoparticles with a spherical shape, but can additionally be used to accurately determine mass, and hence size distributions, of non-spherical and anisotropic nanoparticles [45, 46].

SP-ICP-MS of nanoparticle aggregates

Since SP-ICP-MS was able to determine nanoparticle mass in mixtures and of different sizes, we determined whether we could quantify aggregation of our colloidal nanoparticles with single-particle (i.e., single aggregate) resolution using SP-ICP-MS. We defined aggregation as an irreversible process that results in nanoparticle clusters of two or more individual nanoparticles. To generate aggregates of AuNPs, we exposed citrate-coated 16-nm AuNP model nanoparticles with narrow size distribution to physiologically relevant saline concentrations (~ 150 mM NaCl). Upon exposure to high ionic strength conditions, electrostatically stabilized citrate-coated AuNPs experience substantial screening of their overall negative surface charges [47]. The process of ionic strength–mediated surface charge screening causes colloidal citrate-coated AuNPs to irreversibly aggregate [48]. Aggregation of AuNPs results in a visible color change from red to blue. Using UV-Vis spectrophotometry, we monitored aggregation kinetics of citrate-coated 16-nm AuNPs exposed to 150 mM NaCl over a time period of 60 min (ESM Fig. S4). The observed increase in AuNP light absorption around 600 nm over time (~ 110% change after 60 min, ESM Fig. S4) is due to surface plasmon resonance (SPR) frequency changes as a result of AuNP aggregation. Additional DLS measurements confirmed the observed nanoparticle aggregation behavior with increases in hydrodynamic diameter and PDI and verified our UV-Vis spectrophotometry results (Table S4). We further performed TEM to visualize the aggregation of citrate-coated 16-nm AuNPs upon addition of 150 mM NaCl (ESM Fig. S5).

After establishing the aggregation characteristics and kinetics of citrate-coated 16-nm AuNPs with UV-Vis spectrophotometry and DLS batch methods, we quantified the corresponding aggregation states with SP-ICP-MS at the individual aggregate level. First, AuNP aggregates were formed under the same conditions used for UV-Vis and DLS analysis. Immediately prior to SP-ICP-MS analysis, AuNPs in the NaCl solution were diluted with nanopure water to obtain an AuNP concentration of $1.66 \times$

10^{-16} M which mitigated potential matrix effects from NaCl and maintained the integrity of AuNP aggregates. It is unlikely that the attractive van der Waals forces that bind the nanoparticles in an aggregated state would be compromised to make nanoparticle aggregates fall apart [49]. Given that the mean mass of our monodisperse 16-nm AuNPs was determined to be 50 ag (Fig. 2), we assumed that 100 ag corresponded to an aggregate consisting of 2 AuNPs, 150 ag corresponded to an aggregate consisting of 3 nanoparticles, and so forth, according to Eq. 2. It is important to note that in Fig. 2, few particles had a mass above 100 ag. In our study, the probability of detecting an individual nanoparticle with a true mass above 100 ag rather than an aggregate was only ~2% due to the narrow size distribution of our engineered nanoparticles.

$$N_{\text{NPs per Aggregate}} = \frac{m_{\text{Aggregate}}}{m_{\text{NP}}} \qquad (2)$$

with $N_{\text{NPs per Aggregate}}$ as the number of nanoparticles (NPs) per aggregate, $m_{\text{Aggregate}}$ as the detected mass for an event, i.e., aggregate, ≥ 100 ag, and m_{NP} as the mean mass of an individual 16-nm AuNP (i.e., 50 ag).

As shown in the mass histogram in Fig. 4a, citrate-coated 16-nm AuNPs exhibited a slight increase in mass upon exposure to saline solution in as little as 5 min. (Note: 5 min after salt exposure was the earliest time point that we could physically acquire due to the time required for AuNP sample dilution and introduction into the ICP-MS). However, after 60 min, multiple events with masses ≥ 200 ag were detected. These higher masses indicated the generation and presence of AuNP aggregates. From the mass histograms, we quantified the number of nanoparticles per aggregate at the two time points (Fig. 4b). Interestingly, the number of aggregates consisting of 2 and 3 nanoparticles was the most frequent aggregates after 60 min. It appeared that the generation of AuNP aggregates occurred within 5 min, as the number of single individual particles slightly decreased by ~6% while the masses corresponding to 2 and 3 nanoparticles per aggregate slightly increased by ~6% (Fig. 4c). This increase in number of aggregates was clearly seen after 60 min where the number of detected individual single AuNPs decreased by 70% when compared with AuNPs in the initial measurement without saline. The number of events with masses $\geq$ 100 ag was calculated to be ~73% out of the total events detected (Fig. 4c). Within this group, more than half (52%) were comprised of 2–5 AuNPs per aggregate while only ~ 21% of the detected aggregates consisted of 5 or more AuNPs (Fig. 4d). This result indicated that the formation of larger aggregates could depend on the initial generation kinetics and frequency of smaller AuNP aggregates. Our data also suggest that salt-induced AuNP aggregation is irreversible since the frequency of individual nanoparticle masses decreased over time.

Our SP-ICP-MS experiments confirmed the findings from DLS and UV-Vis spectrophotometry and showed the rapid progression of salt-induced AuNP aggregation. However, in stark contrast to ensemble methods and other single-particle techniques, we could determine individual masses of AuNP aggregates in situ without the need for harsh sample preparation conditions as is required for electron microscopy. When compared with light scattering techniques, SP-ICP-MS results were not skewed by larger nanoparticles and did not account for the extra layer of hydration, as we only measured the gold atoms/ions of the AuNPs. In summary, SP-ICP-MS allowed high-throughput quantitative analysis (200+ aggregates per minute) making it an attractive tool to monitor and study nanoparticle aggregation characteristics.

SP-ICP-MS of surface-modified gold nanoparticles

To mitigate nanoparticle aggregation, we hypothesized that the PEGylation of colloidal AuNPs, i.e., the decoration of nanoparticle surfaces with polyethylene glycol (PEG) polymers, could be adopted for our study as a robust and efficient nanoparticle surface engineering technique to control and reduce AuNP aggregation upon exposure to physiological saline concentrations. PEG polymers are typically used to provide steric stabilization of nanoparticles to physically reduce nanoparticle aggregation [50–52]. Nanoparticles can be engineered to exhibit different PEG surface densities that affect nanoparticle colloidal stability and functionality upon environmental and biological exposure [53, 54]. We prepared 16-nm AuNPs modified with various surface densities of thiol-PEG5kDa-methoxy and summarized our AuNP physicochemical characterization results in the ESM (Fig. S6). Increasing PEG densities led to increases in hydrodynamic diameter and zeta potential, and decreases in nanoparticle mobility in gel electrophoresis. Our results demonstrated that the AuNPs with varying degrees of PEG were monodisperse without any detectable aggregation (i.e., PDI < 0.1, ESM Fig. S6). We then tested if the amount of PEG added on the AuNP surface played a role in colloidal stability and aggregation. We want to emphasize that the amount of PEG added to AuNPs does not necessarily represent the amount of PEG attached to AuNPs.

We exposed the PEGylated AuNPs to 150 mM NaCl and measured the corresponding UV-Vis absorption spectra over the course of 60 min. In stark contrast to citrate-coated 16-nm AuNPs (ESM Fig. S4C), we observed only a small increase (~10%) in light absorption at 600 nm over a time period of 60 min for PEGylated AuNPs (0.010 PEG per nm^2 of nanoparticle surface area corresponding to ~6 PEG polymers per AuNP) upon exposure to 150 mM NaCl (ESM Fig. S4B, S4C). This observation was confirmed by DLS measurements that showed a small increase in hydrodynamic diameter of ~ 3 nm and a more pronounced fourfold increase in PDI indicative of slight nanoparticle aggregation (Table S4). It is worth noting that under the same experimental conditions, AuNPs with higher PEG surface densities (i.e., 0.025 PEG/nm^2 and

Fig. 4 SP-ICP-MS to assess citrate-coated AuNP aggregation. **a** Mass histograms of citrate-coated 16-nm colloidal AuNPs exposed to 150 mM aqueous NaCl solution over time. **b** Detected mass distribution in panel **a** is converted into number of nanoparticles per aggregate (bin size = 50 ag). **c** Percentage of individual nanoparticles are compared with masses > 100 ag, a mass which is equal to > 2 nanoparticles per aggregate (i.e., detected event). **d** Breakdown of AuNP aggregates into bins of 2–5 and > 5 AuNPs per aggregate (i.e., detected event)
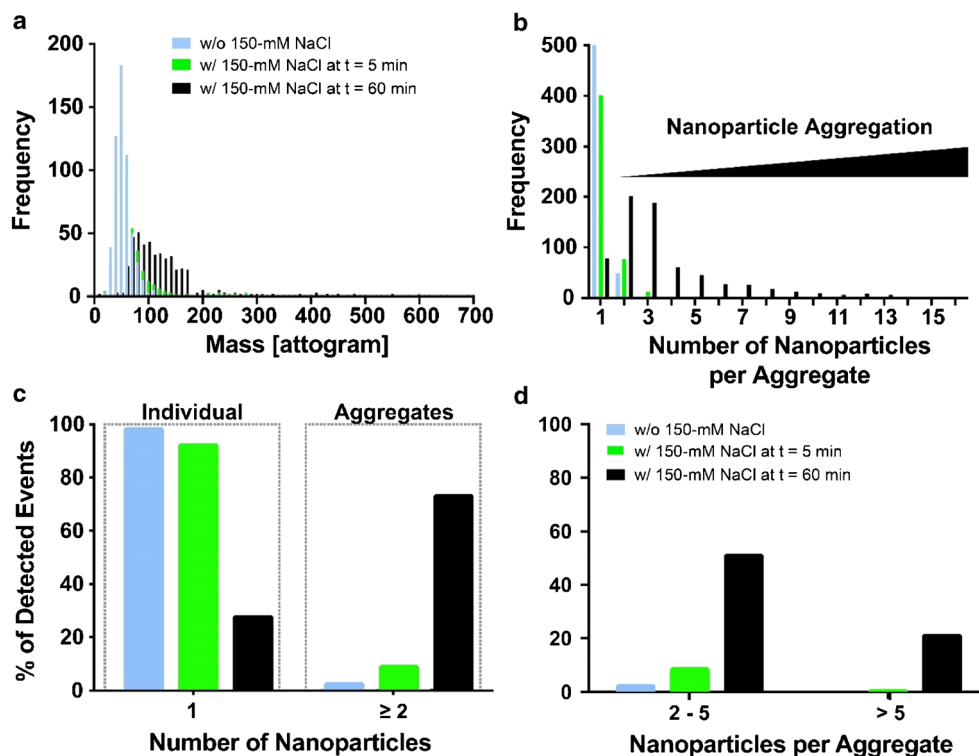

0.050 PEG/nm^2) were less affected by aggregation as demonstrated by UV-Vis spectrophotometry (data not shown) and DLS measurements (Table S4). Based on our collective UV-Vis spectrophotometry and DLS results, we concluded that PEGylation of 16-nm AuNPs, even at PEG surface densities of only 6–30 PEG molecules per AuNP, effectively reduced nanoparticle aggregation upon exposure to physiologically relevant NaCl concentrations (ESM, Table S4 and Fig. S4).

To obtain a deeper understanding of the reduced aggregation behavior seen with DLS and UV-Vis spectrophotometry, we used SP-ICP-MS to obtain mass distributions of the PEGylated AuNPs exposed to saline solution (Fig. 5). The masses of the PEGylated AuNPs after 5 min primarily exhibited masses below 100 ag (Fig. 5a). Interestingly, AuNPs with the lowest PEG surface density (0.010 PEG/nm^2) exhibited a small (~ 10%) decrease in the number of single nanoparticles similar to the AuNPs with 0 PEG/nm^2 (Fig. 5c). On the other hand, AuNPs with higher densities of PEG, such as 0.025 PEG/nm^2, only experienced a ~ 5% decrease in observed single particles. Meanwhile, AuNPs with the highest density of PEG (0.050 PEG/nm^2) had only ~ 2% of all detected events above 100 ag similar to what was observed for AuNPs in Fig. 2 without exposure to salt. These findings corroborated our observations that the onset nanoparticle aggregation occurred within 5 min after saline exposure. In addition, surface modifications like PEG can be used to physically hinder the rapid onset of salt-induced aggregation in a PEG surface density–dependent fashion. For a more concise comparison, the mean masses and standard deviations of the PEGylated AuNPs in saline solutions are shown in ESM Fig. S7.

As the effects of aggregation were time dependent as shown in Fig. 4, and in ESM Fig. S6 and Table S4, we analyzed the PEGylated AuNPs in saline solution, after 60 min via SP-ICP-MS. Upon analysis, we observed that 98% of all detected events for the PEGylated AuNPs had masses below 150 ag (Fig. 5b). Remarkably, AuNPs modified with 0.050 PEG/nm^2 had twofold less events above 150 ag when compared with the AuNPs with 0.010 and 0.025 PEG/nm^2. This finding indicated that the formation of larger aggregates (3 or more nanoparticles) was virtually completely inhibited by PEG. After 60 min in saline, more than 90% of all detected events were detected as individual nanoparticles for each PEG surface density compared with the 27% of individual nanoparticles observed for citrate-coated AuNPs (Fig. 5d). AuNPs modified with 0.010 and 0.025 PEG/nm^2 had similar amounts of masses > 100 ag (~ 6% out of all detected events). On the other hand, for AuNPs modified with 0.050 PEG/nm^2, 97% of detected events were below a mass of 100 ag indicating negligible (if any) aggregation in the saline solution after 60 min. For AuNPs with 0.050 PEG/nm^2, the number of events with masses > 100 ag was nearly identical to the baseline of observed events with true masses > 100 ag at both t_{5min} and t_{60min} indicating that high PEG surface densities preserved the monodisperse character and colloidal stability of AuNPs in saline conditions over time. Our SP-ICP-MS results for the PEGylated AuNPs were corroborated by DLS measurements in ESM Table S4 that showed lower PEG surface (0.010 and 0.025 PEG/nm^2) had PDI > 0.1, while only the AuNPs with 0.050 PEG/nm^2 had a PDI < 0.1 after 60 min in saline

Fig. 5 SP-ICP-MS to evaluate aggregation characteristics of PEGylated 16-nm AuNPs exposed to 150 mM NaCl. Mass histograms of PEGylated 16-nm AuNPs at t_{5min} in saline solution (**a**) and t_{60min} in saline solution (**b**). Percentages of individual nanoparticles of total detected nanoparticle events are plotted at t_{5min} (**c**) and t_{60min} (**d**) for PEGylated AuNPs in 150 mM NaCl
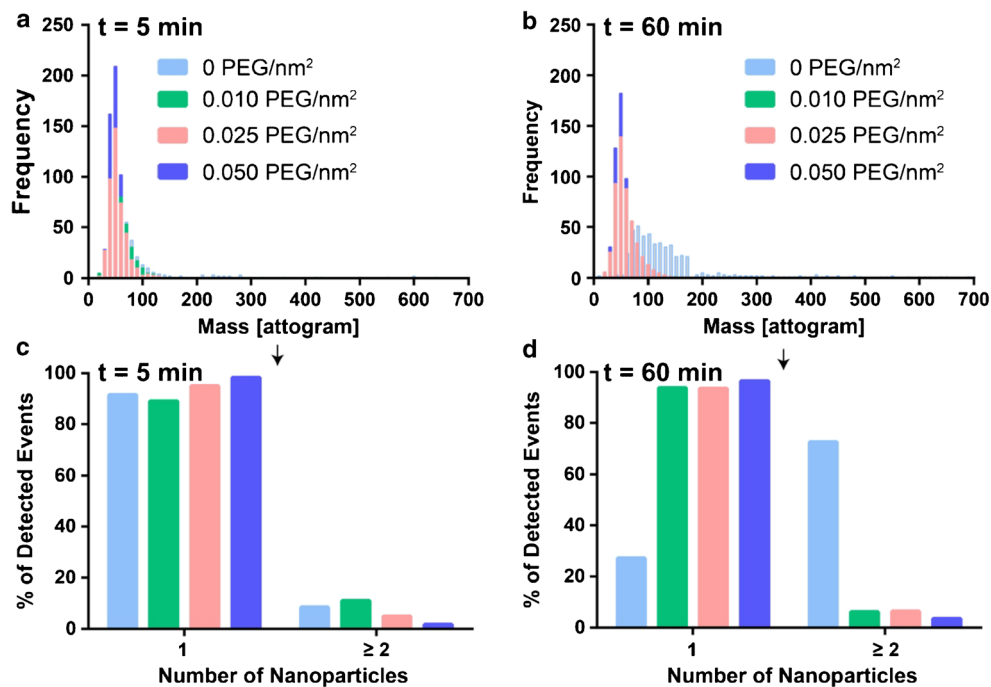
solution. Our SP-ICP-MS findings confirmed that, based on our testing conditions, the addition of as little as 0.010 PEG/nm² was sufficient for reducing the time-dependent effects of aggregation for monodisperse 16-nm model AuNPs. Moreover, our results indicated that higher PEG surface densities better passivate AuNPs to reduce nanoparticle aggregation likely due to improved steric stabilization by neutral PEG polymers.

Conclusions

We established and validated SP-ICP-MS as a viable quantitative high-throughput analytical technique that enables the rapid and precise measurement of engineered nanomaterials with single-particle resolution. Our SP-ICP-MS results were corroborated by both conventional ensemble nanoparticle characterization methods, such as UV-Vis spectrophotometry and DLS, as well as the single-particle data from TEM. With our SP-ICP-MS approach, we were able to precisely detect and quantify the heterogeneity of AuNPs with high throughput (200+ nanoparticles/min) and recovery (> 90%). Additionally, we used SP-ICP-MS to accurately quantify AuNPs with various shapes and different nanoparticle size populations from nanoparticle mixtures. Furthermore, we applied SP-ICP-MS as an in situ technique to quantify the colloidal stability of AuNPs in physiologically relevant saline conditions and showed the mass distributions of AuNP aggregates with single aggregate resolution. Through rational surface engineering strategies, we demonstrated that increasing nanoparticle PEG surface densities could efficiently attenuate irreversible nanoparticle aggregation through steric stabilization. The work presented in this study has potential far-reaching implications for researchers who seek to understand how engineered nanoparticles aggregate over time in biologically relevant environments and how surface modifications affect nanoparticle colloidal stability.

Compliance with ethical standards

Conflict of interest The authors declare that they have no conflict of interest.

Disclaimer The content is solely the responsibility of the authors and does not necessarily represent the official views of the Oklahoma Tobacco Settlement Endowment Trust.

References

1. Pelaz B, Alexiou C, Alvarez-Puebla RA, et al. Diverse applications of nanomedicine. ACS Nano. 2017;11:2313–81. https://doi.org/10.1021/acsnano.6b06040.

2. Wilhelm S. Perspectives for upconverting nanoparticles. ACS Nano. 2017;11:10644–53.

3. Narum SM, Le T, Le DP, et al. Passive targeting in nanomedicine: fundamental concepts, body interactions, and clinical potential. In: Nanoparticles for Biomedical Applications: Elsevier; 2020. p. 37–53.

4. Albanese A, Walkey CD, Olsen JB, et al. Secreted biomolecules alter the biological identity and cellular interactions of nanoparticles. ACS Nano. 2014;8:5515–26. https://doi.org/10.1021/nn4061012.

5. Wilhelm S, Tavares AJ, Dai Q, et al. Analysis of nanoparticle delivery to tumours. Nat Rev Mater. 2016;1:1–12.

6. Poon W, Zhang YN, Ouyang B, et al. Elimination pathways of nanoparticles. ACS Nano. 2019;13:5785–98. https://doi.org/10.1021/acsnano.9b01383.

7. Donahue ND, Acar H, Wilhelm S. Concepts of nanoparticle cellular uptake, intracellular trafficking, and kinetics in nanomedicine. Adv Drug Deliv Rev. 2019;143. https://doi.org/10.1016/j.addr.2019.04.008.

8. Modena MM, Rühle B, Burg TP, Wuttke S. Nanoparticle characterization: what to measure? Adv Mater. 2019;31:1901556. https://doi.org/10.1002/adma.201901556.

9. Marquis BJ, Love SA, Braun KL, Haynes CL. Analytical methods to assess nanoparticle toxicity. Analyst. 2009;134:425–39.

10. Hoo CM, Starostin N, West P, Mecartney ML. A comparison of atomic force microscopy (AFM) and dynamic light scattering (DLS) methods to characterize nanoparticle size distributions. J Nanopart Res. 2008;10:89–96. https://doi.org/10.1007/s11051-008-9435-7.

11. Olson J, Dominguez-Medina S, Hoggard A, et al. Optical characterization of single plasmonic nanoparticles. Chem Soc Rev. 2015;44:40–57.

12. Montaño MD, Lowry GV, Blue J. Current status and future direction for examining engineered nanoparticles in natural systems. 2010. https://doi.org/10.1071/EN14037.

13. Brar SK, Verma M. Measurement of nanoparticles by light-scattering techniques. TrAC - Trends Anal Chem. 2011;30:4–17.

14. Dastanpour R, Boone JM, Rogak SN. Automated primary particle sizing of nanoparticle aggregates by TEM image analysis. Powder Technol. 2016;295:218–24. https://doi.org/10.1016/j.powtec.2016.03.027.

15. Filipe V, Hawe A, Jiskoot W. Critical evaluation of nanoparticle tracking analysis (NTA) by NanoSight for the measurement of nanoparticles and protein aggregates. Pharm Res. 2010;27:796–810. https://doi.org/10.1007/s11095-010-0073-2.

16. Montaño MD, Olesik JW, Barber AG, et al. Single particle ICP-MS: advances toward routine analysis of nanomaterials. Anal Bioanal Chem. 2016;408:5053–74. https://doi.org/10.1007/s00216-016-9676-8.

17. Mozhayeva D, Engelhard C. A critical review of single particle inductively coupled plasma mass spectrometry – a step towards an ideal method for nanomaterial characterization. J Anal At Spectrom. 2020. https://doi.org/10.1039/c9ja00206e.

18. Corte Rodríguez M, Álvarez-Fernández García R, Blanco E, et al. Quantitative evaluation of cisplatin uptake in sensitive and resistant individual cells by single-cell ICP-MS (SC-ICP-MS). Anal Chem. 2017;89:11491–7. https://doi.org/10.1021/acs.analchem.7b02746.

19. Wilhelm S, Bensen RC, Kothapali NR, et al (2018) Quantification of gold nanoparticle uptake into cancer cells using single cell ICP-MS. PerkinElmer Appl Note.

20. Lee JC, Donahue ND, Mao AS, et al. Exploring maleimide-based nanoparticle surface engineering to control cellular interactions. ACS Appl Nano Mater. 2020;3:2421–9. https://doi.org/10.1021/acsanm.9b02541.

21. Albanese A, Tang PS, Chan WCW. The effect of nanoparticle size, shape, and surface chemistry on biological systems. Annu Rev Biomed Eng. 2012;14:1–16. https://doi.org/10.1146/annurev-bioeng-071811-150124.

22. Wilhelm S, Kaiser M, Würth C, et al. Water dispersible upconverting nanoparticles: effects of surface modification on their luminescence and colloidal stability. Nanoscale. 2015;7:1403–10. https://doi.org/10.1039/c4nr05954a.

23. Muhr V, Wilhelm S, Hirsch T, Wolfbeis OS. Upconversion nanoparticles: from hydrophobic to hydrophilic surfaces. Acc Chem Res. 2014;47:3481–93. https://doi.org/10.1021/ar500253g.

24. Hassellöv M, Readman JW, Ranville JF, Tiede K. Nanoparticle analysis and characterization methodologies in environmental risk assessment of engineered nanoparticles. Ecotoxicology. 2008;17:344–61.

25. Love SA, Maurer-Jones MA, Thompson JW, et al. Assessing nanoparticle toxicity. Annu Rev Anal Chem. 2012;5:181–205. https://doi.org/10.1146/annurev-anchem-062011-143134.

26. Buchman JT, Hudson-Smith NV, Landy KM, Haynes CL. Understanding nanoparticle toxicity mechanisms to inform redesign strategies to reduce environmental impact. Acc Chem Res. 2019;52:1632–42. https://doi.org/10.1021/acs.accounts.9b00053.

27. Albanese A, Chan WCW. Effect of gold nanoparticle aggregation on cell uptake and toxicity. ACS Nano. 2011;5:5478–89. https://doi.org/10.1021/nn2007496.

28. Maurer-Jones MA, Lin YS, Haynes CL. Functional assessment of metal oxide nanoparticle toxicity in immune cells. ACS Nano. 2010;4:3363–73. https://doi.org/10.1021/nn9018834.

29. Maurer-Jones MA, Gunsolus IL, Murphy CJ, Haynes CL. Toxicity of engineered nanoparticles in the environment. Anal Chem. 2013;85:3036–49. https://doi.org/10.1021/ac303636s.

30. Kim HA, Lee BT, Na SY, et al. Characterization of silver nanoparticle aggregates using single particle-inductively coupled plasma-mass spectrometry (spICP-MS). Chemosphere. 2017;171:468–75. https://doi.org/10.1016/j.chemosphere.2016.12.063.

31. Perrault SD, Warren CWC. Synthesis and surface modification of highly monodispersed, spherical gold nanoparticles of 50−200 nm. J Am Chem Soc. 2009;131:17042–3. https://doi.org/10.1021/ja907069u.

32. Vigderman L, Zubarev ER. High-yield synthesis of gold nanorods with longitudinal SPR peak greater than 1200 nm using hydroquinone as a reducing agent. Chem Mater. 2013;25:1450–7. https://doi.org/10.1021/cm303661d.

33. Zhou S, Huo D, Goines S, et al. Enabling complete ligand exchange on the surface of gold nanocrystals through the deposition and then etching of silver. J Am Chem Soc. 2018;140:11898–901. https://doi.org/10.1021/jacs.8b06464.

34. Merrifield RC, Stephan C, Lead JR. Quantification of Au nanoparticle biouptake and distribution to freshwater algae using single cell - ICP-MS. Environ Sci Technol. 2018;52:2271–7. https://doi.org/10.1021/acs.est.7b04968.

35. Corte-Rodríguez M, Blanco-González E, Bettmer J, Montes-Bayón M. Quantitative analysis of transferrin receptor 1 (TfR1) in individual breast cancer cells by means of labeled antibodies and elemental (ICP-MS) detection. Anal Chem. 2019;91:15532–8. https://doi.org/10.1021/acs.analchem.9b03438.

36. Mavrakis E, Mavroudakis L, Lydakis-Simantiris N, Pergantis SA. Investigating the uptake of arsenate by Chlamydomonas reinhardtii cells and its effect on their lipid profile using single cell ICP-MS and easy ambient sonic-spray ionization-MS. Anal Chem. 2019;91:9590–8. https://doi.org/10.1021/acs.analchem.9b00917.

37. Cuello-Nuñez S, Abad-Álvaro I, Bartczak D, et al. The accurate determination of number concentration of inorganic nanoparticles using spICP-MS with the dynamic mass flow approach. J Anal At Spectrom. 2020. https://doi.org/10.1039/c9ja00415g.

38. Pace HE, Rogers NJ, Jarolimek C, et al. Determining transport efficiency for the purpose of counting and sizing nanoparticles via single particle inductively coupled plasma mass spectrometry. Anal Chem. 2011;83:9361–9. https://doi.org/10.1021/ac201952t.

39. Pace HE, Rogers NJ, Jarolimek C, et al. Single particle inductively coupled plasma-mass spectrometry: a performance evaluation and method comparison in the determination of nanoparticle size. Environ Sci Technol. 2012;46:12272–80. https://doi.org/10.1021/es301787d.

40. Kang H, Buchman JT, Rodriguez RS, et al. Stabilization of silver and gold nanoparticles: preservation and improvement of plasmonic functionalities. Chem Rev. 2019;119:664–99.

41. Muhammad Syed A, Sindhwani S, Wilhelm S, et al. Three-dimensional imaging of transparent tissues via metal nanoparticle labeling. J Am Chem Soc. 2017;139:9961–71. https://doi.org/10.1021/jacs.7b04022.

42. Haiss W, Thanh NTK, Aveyard J, Fernig DG. Determination of size and concentration of gold nanoparticles from UV-Vis spectra. Anal Chem. 2007;79:4215–21. https://doi.org/10.1021/ac0702084.

43. Hineman A, Stephan C. Effect of dwell time on single particle inductively coupled plasma mass spectrometry data acquisition quality. J Anal At Spectrom. 2014;29:1252–7. https://doi.org/10.1039/c4ja00097h.

44. Lee S, Bi X, Reed RB, et al. Nanoparticle size detection limits by single particle ICP-MS for 40 elements. Environ Sci Technol. 2014;48:10291–300. https://doi.org/10.1021/es502422v.

45. Tan J, Yang Y, El Hadri H, et al. Fast quantification of nanorod geometry by DMA-spICP-MS. Analyst. 2019;144:2275–83. https://doi.org/10.1039/c8an02250j.

46. Kálomista I, Kéri A, Ungor D, et al. Dimensional characterization of gold nanorods by combining millisecond and microsecond temporal resolution single particle ICP-MS measurements. J Anal At Spectrom. 2017;32:2455–62. https://doi.org/10.1039/c7ja00306d.

47. Christau S, Moeller T, Genzer J, et al. Salt-induced aggregation of negatively charged gold nanoparticles confined in a polymer brush matrix. Macromolecules. 2017;50:7333–43. https://doi.org/10.1021/acs.macromol.7b00866.

48. Pamies R, Cifre JGH, Espín VF, et al. Aggregation behaviour of gold nanoparticles in saline aqueous media. J Nanopart Res. 2014;16. https://doi.org/10.1007/s11051-014-2376-4.

49. Kim T, Lee CH, Joo SW, Lee K. Kinetics of gold nanoparticle aggregation: experiments and modeling. J Colloid Interface Sci. 2008;318:238–43. https://doi.org/10.1016/j.jcis.2007.10.029.

50. Suk JS, Xu Q, Kim N, et al. PEGylation as a strategy for improving nanoparticle-based drug and gene delivery. Adv Drug Deliv Rev. 2016;99:28–51.

51. Jokerst JV, Lobovkina T, Zare RN, Gambhir SS. Nanoparticle PEGylation for imaging and therapy. Nanomedicine. 2011;6:715–28.

52. Manson J, Kumar D, Meenan BJ, Dixon D. Polyethylene glycol functionalized gold nanoparticles: the influence of capping density on stability in various media. Gold Bull. 2011;44:99–105. https://doi.org/10.1007/s13404-011-0015-8.

53. Zhang XD, Wu D, Shen X, et al. Size-dependent in vivo toxicity of PEG-coated gold nanoparticles. Int J Nanomedicine. 2011;6:2071–81. https://doi.org/10.2147/ijn.s21657.

54. Walkey CD, Olsen JB, Guo H, et al. Nanoparticle size and surface chemistry determine serum protein adsorption and macrophage uptake. J Am Chem Soc. 2012;134:2139–47. https://doi.org/10.1021/ja2084338.

Nathan D. Donahue is a PhD graduate student in Prof. Stefan Wilhelm's group at the Stephenson School of Biomedical Engineering (University of Oklahoma). In his research, he applies elemental analysis techniques to understand interactions between engineered nanoparticles and biological systems.

Emmy R. Francek is a biomedical engineering undergraduate student in Prof. Stefan Wilhelm's group at the University of Oklahoma. She focuses on the synthesis and characterization of nanoparticles for drug delivery applications.


Emi Kiyotake is a PhD candidate in Prof. Michael Detamore's group in the Stephenson School of Biomedical Engineering at the University of Oklahoma. Her research focuses on the development and application of conductive and injectable hydrogels for nerve repair after spinal cord injury.


Emily E. Thomas is a biomedical engineering undergraduate student in Prof. Michael Detamore's group at the University of Oklahoma where she focuses on biomaterials research for regenerative medicine.

Wen Yang is a PhD graduate student in Prof. Stefan Wilhelm's group at the Stephenson School of Biomedical Engineering (University of Oklahoma). In her research, she focuses on nanoparticle surface engineering strategies for efficient drug delivery.
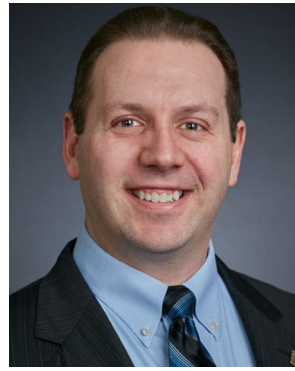
Michael S. Detamore is the Founding Director, Stephenson Chair #1, and Professor in the Stephenson School of Biomedical Engineering at the University of Oklahoma. He has developed a variety of new biomaterials for the application of translational regenerative medicine.
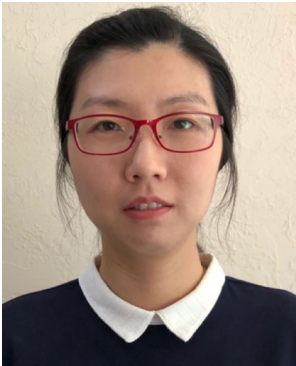
Lin Wang is a postdoctoral fellow in Prof. Stefan Wilhelm's group at the Stephenson School of Biomedical Engineering (University of Oklahoma). In her research, she focuses on developing new nanoparticle engineering strategies to improve nanomedicine.

Stefan Wilhelm is an Assistant Professor at the Stephenson School of Biomedical Engineering (University of Oklahoma). His research is focused on bioanalytical chemistry and the study of nano-bio interactions for the development of next-generation nanomedicines.